



**HAL**  
open science

## 10 Be exposure age for sorted polygons in the Sudetes Mountains

Zbyněk Engel, Marek Křížek, Regis Braucher, Tomáš Uxa, David Krause

► **To cite this version:**

Zbyněk Engel, Marek Křížek, Regis Braucher, Tomáš Uxa, David Krause. 10 Be exposure age for sorted polygons in the Sudetes Mountains. *Permafrost and Periglacial Processes*, 2021, 32 (1), pp.154-168. 10.1002/ppp.2091 . hal-03008882

**HAL Id: hal-03008882**

**<https://hal.science/hal-03008882>**

Submitted on 17 Nov 2020

**HAL** is a multi-disciplinary open access archive for the deposit and dissemination of scientific research documents, whether they are published or not. The documents may come from teaching and research institutions in France or abroad, or from public or private research centers.

L'archive ouverte pluridisciplinaire **HAL**, est destinée au dépôt et à la diffusion de documents scientifiques de niveau recherche, publiés ou non, émanant des établissements d'enseignement et de recherche français ou étrangers, des laboratoires publics ou privés.

1 **<sup>10</sup>Be exposure age for sorted polygons in the Sudetes Mountains**

2 Zbyněk Engel<sup>a,\*</sup>, Marek Křížek<sup>a</sup>, Régis Braucher<sup>b</sup>, Tomáš Uxa<sup>ac</sup>, David Krause<sup>ad</sup>, AsterTeam<sup>b</sup>

3

4 <sup>a</sup> Charles University, Faculty of Science, Department of Physical Geography and Geoecology,  
5 Prague, Czech Republic

6 <sup>b</sup> CEREGE CNRS Aix Marseille Univ., IRD, INRAE, Collège de France, Aix-en-Provence,  
7 France

8 <sup>c</sup> Academy of Sciences of the Czech Republic, Institute of Geophysics, Department of  
9 Geothermics, Prague, Czech Republic

10 <sup>d</sup> The Krkonoše Mountains National Park Administration, Vrchlabí, Czech Republic

11 AsterTeam: Georges Aumaître, Didier Bourlès, Karim Keddadouche

12 \* Corresponding author. Tel.: +420 22 195 1373. E-mail address: [engel@natur.cuni.cz](mailto:engel@natur.cuni.cz).

13

14 **Abstract**

15 Patterned ground landforms represent the most common phenomenon of periglacial  
16 environment and its large sorted forms belong to the few morphological indicators of former  
17 permafrost distribution. Relic forms of patterned ground are widespread on high-elevated  
18 surfaces in the central European uplands, providing the evidence of regional periglacial  
19 conditions in the past. However, the timing of these landforms as well as their potential for  
20 paleoclimate reconstructions, have remained unexplored. In this paper, we present <sup>10</sup>Be  
21 exposure ages from the large sorted polygons sampled at four sites in the Sudetes Mountains,  
22 the highest part of the central European uplands. These results indicate that these landforms  
23 started to form at the end of MIS 3 and the main phase of their formation occurred between 30  
24 and 20 ka. This research confirms the hypothesis of patterned ground formation within the  
25 Weichselian glacial (115ka-10ka ?) and suggests that earlier landforms are not preserved in  
26 the Sudetes. The recognised period of enhanced periglacial activity coincides with a  
27 prominent cold interval identified earlier in both regional and northern-hemispheric proxy  
28 records.

29 **1 Introduction**

30 Cryogenic sorted patterned ground refers to the arrangement of segregated fine and coarse  
31 material that form at the ground surface as a result of differential frost heave and buoyancy-  
32 driven soil circulation.<sup>1</sup> The resulting forms are more or less symmetric features among which  
33 circles and polygons are most common. The polygonal pattern reflects uneven penetration of  
34 freezing planes into the ground, displacement of clasts from concentrations of finer soil  
35 toward pattern margins, and lateral interaction of adjacent fine cells.<sup>2</sup> Small-scaled circles and  
36 polygons (<1m in diameter) form in seasonally-frozen ground, but larger sorted forms are  
37 found only in areas underlain by permafrost.<sup>3</sup> Relict forms of large sorted forms thus provide  
38 evidence for the former existence of permafrost and allow rough estimates of paleoclimatic  
39 conditions.<sup>4</sup>

40 The distribution of cryogenic sorted patterned ground has been frequently used for spatial  
41 reconstructions of periglacial environment during the cold stages of the Quaternary as their  
42 distinct pattern can be easily identified in the field and remotely sensed data. Moreover,  
43 dimensions of large (> 1 m wide) sorted forms of patterned ground indicate the thickness of  
44 former active-layer that corresponds to the depth of sorting and landform width.<sup>5</sup> The  
45 paleoclimatic interpretation of patterned ground has been mostly considered limited because  
46 of the complex history of their formation and the possible influence of non-climate-related  
47 local factors.<sup>6</sup> However, large sorted forms indicate lack of a thick snow cover, frequent  
48 freeze-thaw cycles, and air temperature thresholds required for differential sorting and frost-  
49 heave.<sup>7</sup> Nowadays, large sorted forms of patterned ground are active in the permafrost areas  
50 with mean annual air temperature (MAAT) lower than  $-6\text{ }^{\circ}\text{C}$  to  $-3\text{ }^{\circ}\text{C}$ .<sup>8,9</sup> Hence, these  
51 landforms can, when constrained by geochronological data, provide insights into Quaternary  
52 climatic conditions.

53

54 Unfortunately, there is still no robust approach for the dating of patterned ground, despite the  
55 recent advances in geochronology. The main problem for dating these structures results from  
56 the complex history of their formation as they can develop over a short/long time span and/or  
57 during multiple cold events.<sup>10</sup> Large sorted polygons are products of recurrent freezing and  
58 thawing of the active layer, which causes upward movements of coarse clasts from the  
59 permafrost table and their subsequent migration towards the margins of the polygons.<sup>11, 12</sup>  
60 Under prolonged freeze-thaw conditions, the boulders forming the margins may be tilted due

61 to lateral squeezing of adjacent polygons.<sup>13</sup> Although this process can shorten the exposure  
62 age of the boulders it still represents the period of polygon formation. If the frequency of  
63 freeze-thaw cycles drops back to the non-permafrost conditions, the supply of clasts via frost  
64 heave and lateral sorting ceases and large boulders at the margin of the polygons stabilize,  
65 attesting to the last time of their activity. Smaller pattern may eventually form in the centre of  
66 the inactive polygons at a later time if environmental conditions become suitable.<sup>3</sup>

67 Since the 1990s, radiocarbon, luminescence and terrestrial *in situ*-produced cosmogenic  
68 nuclides (TCN) dating methods have been applied on patterned-ground forms to determine  
69 their ages. Radiocarbon ages were reported mostly for non-sorted patterned ground, especially  
70 earth hummocks, rich in organics.<sup>14</sup> Only few radiocarbon data were obtained for sorted  
71 patterned ground<sup>15-17</sup> that usually contains a small amount of organic material. Moreover, this  
72 material may have formed earlier or later than the landform itself.<sup>16</sup> Thermoluminescence and  
73 optically stimulated luminescence (OSL) dating has been used for the dating of non-sorted  
74 circles, stripes and polygons<sup>18-20</sup> but a successful application remains challenging.<sup>21</sup> Apart  
75 from the issues related to the polycyclic nature of these features,<sup>19</sup> the possible incorporation  
76 of incompletely bleached grains, and fluctuations of the water content after sedimentation of  
77 the material complicates the interpretation of the luminescence data.<sup>22</sup> The application of TCN  
78 in the dating of patterned ground is still rare. The method has only been used to estimate the  
79 timing of poorly sorted patterns based on the dating of underlying rock glaciers.<sup>23, 24</sup> [and to](#)  
80 [obtain Schmidt-hammer exposure ages for sorted circles and stripes.](#)<sup>6, 25</sup> The most frequent  
81 applications of TCN in the periglacial landscape include the determination of ‘periglacial  
82 trimlines’,<sup>26</sup> the timing of rock glaciers<sup>27</sup> and boulder fields.<sup>28</sup>

83 In this paper, we aim at constraining the timing of sorted polygons in the Sudetes Mountains,  
84 the highest section of the central European uplands. This region is characterized by large  
85 surfaces of low relief above 1200 m a.s.l. (referred to as summit planation surfaces in this  
86 paper)<sup>29</sup> with well-developed periglacial landforms. Among these landforms, sorted patterned  
87 ground phenomena were recognised first because of their distinctive morphology and  
88 widespread distribution.<sup>30</sup> An earlier hypothesis relates their origin with past glacial cycles  
89 and attributes most of the preserved forms to the culmination phase of the last glacial period.<sup>31</sup>  
90 An alternative view suggests that most patterned ground in the Sudetes formed during the  
91 Lateglacial period.<sup>32</sup> In either case, the chronology of these landforms and paleoclimatic  
92 conditions during the period of their formation remain uncertain. In order to constrain the  
93 timing of the formation of large sorted polygons and to infer paleoclimate conditions for this

94 period we have analysed their distribution and morphology in the Krkonoše and Hrubý  
95 Jeseník Mountains, the highest parts of the Sudetes . 24 new <sup>10</sup>Be surface exposure ages from  
96 four sorted polygon assemblages were produced and <sup>1</sup>, , the established chronology was  
97 compared with a local set of exposure ages reported for glacial and periglacial landforms and  
98 with the existing records of paleoenvironmental conditions in central Europe.

Commentaire [Régis1]: Already written three lines before.

## 99 2 Study area

100 The Sudetes Mountains on the Czech/Polish boundary represent a 340 km long eastern section  
101 of the central European uplands that stretch along 50° N. During the Quaternary glaciations,  
102 the Sudetes Mountains were located within the periglacial zone between the Fennoscandian  
103 ice sheet and ice cap over the Alps (Fig. 1, inset). The width of the zone ranged from 430 km  
104 in the Last Glacial Maximum (LGM) to more than 1300 km during the Middle Weichselian  
105 interstadial. Periglacial processes and loess deposition dominated the development of this  
106 zone over cold stadial episodes. An extensive loess deposition belt was formed in the northern  
107 part of the zone while a more scattered loess cover arose at the southern front of the Sudetes  
108 Mountains below 450 m a.s.l.<sup>35</sup> Periglacial processes have been most intense on summit  
109 planation surfaces where the annual precipitations were estimated to range from 500 to 700  
110 mm during the LGM<sup>36</sup> and the MAAT was 7 to 10°C lower than at present.<sup>37</sup> During the last  
111 glaciation, cirque and valley glaciers modified the central part of the ranges<sup>38</sup> but periglacial  
112 landscape has retained larger extent.

113 The Sudetes Mountains are located in a transitional zone between areas dominated by the  
114 oceanic climate and the continental type regimes. The precipitation on summit planation  
115 surfaces decreases from the Krkonoše Mountains in the western part of the Sudetes Mountains  
116 (>1500 mm per year)<sup>39</sup> to the Hrubý Jeseník Mountains near the eastern margin of the range  
117 (1200–1300 mm per year).<sup>40</sup> The MAAT for the period 1961–1990 ranged from 0.4°C at the  
118 Sněžka weather station (1603 m a.s.l.) in the Krkonoše Mountains and 0.9°C at the Praděd  
119 station (1492 m a.s.l.) in the Hrubý Jeseník Mts. to approximately 3°C at an elevation of 1200  
120 m a.s.l.<sup>41</sup> Westerly winds prevail within the Sudetes Mountains transporting snow from the  
121 summit plateaus to leeward slopes.<sup>42</sup>

122 The Krkonoše Mountains comprise a WNW-ESE oriented main (Silesian) ridge built of the  
123 mid-Carboniferous granites (~320–315 Ma) and a parallel southern (Bohemian) ridge at the  
124 contact between the plutonic complex and Neoproterozoic to Lower Palaeozoic metamorphic  
125 rocks.<sup>43</sup> The ridges delimit the relics of high-elevated (1350–1500 m a.s.l.)<sup>44</sup> planation

126 surfaces (Fig. 1a and 2a) formed as a result of slow weathering and long-term denudation that  
127 probably started around 75 Ma.<sup>46</sup> The Hrubý Jeseník Mountains consist of Keprník and Desná  
128 Domes oriented approximately NE-SW (Fig. 1b). Both domes are built by a Cadomian  
129 crystalline basement imbricated with metamorphosed Devonian volcano sedimentary  
130 complexes.<sup>47</sup> The domes have well-developed summit planation surfaces at 1300–1460 m  
131 a.s.l.,<sup>48</sup> which are more extensive in the southern part of the Desná Dome (Fig. 3a). Planation  
132 surfaces in both the Krkonoše and Hrubý Jeseník Mountains are covered with periglacial  
133 deposits among which sorted forms of patterned ground prevail.<sup>45</sup>

134 The four studied sites are located in high-elevated parts of the Sudetes Mountains. Vysoké  
135 Kolo (1509 m a.s.l.), the highest granite elevation in the western Krkonoše Mountains, and  
136 quartzite-dominated Luční hora (1555 m a.s.l.) on the Bohemian Ridge (Fig. 1a) represent the  
137 highest summit planation surface in the Sudetes Mountains. Břidličná hora (1358 m a.s.l.) and  
138 Větrná louka (1250–1270 m a.s.l.) consist of phyllites and represent the southern part of the  
139 Hrubý Jeseník Mountains (Fig. 1b). Břidličná hora belongs to the highest elevations on the  
140 Desná Dome whereas Větrná louka is located on a lowered planation surface on a side ridge  
141 (Fig. 3). Products of *in situ* weathering dominate at all sites and small sections of exposed  
142 bedrock are present only on Luční hora. All sites except Větrná louka are located in the zone  
143 of limited vegetation above the timberline (Fig. 1 and 3e).

### 144 **3 Methods**

#### 145 *3.1 Morphological analyses and boulder sampling*

146 We selected four study sites with the best-developed and undisturbed sorted polygons in the  
147 Sudetes Mountains for morphological analyses and <sup>10</sup>Be sampling. The length, width and  
148 height of the 81 sorted polygons were measured at these sites. The height is defined as the  
149 maximum vertical distance between the lowest point at the polygon border and the highest  
150 point at its updomed centre.<sup>49</sup> Between-site differences in the height and width of the sorted  
151 polygons were assessed by a one-way analysis of variance (ANOVA), and tested using an F-  
152 test at the significance level  $p = 0.05$ . The length of the sorted polygons was excluded from  
153 the ANOVA analyses because this parameter can relate to the surface inclination and thus it  
154 can reflect other factors, such as solifluction.<sup>50</sup> The width of the polygons was used to roughly  
155 estimate the thickness of the past active layer based on the regression equation (Fig. 4) for a  
156 set of published paired data.<sup>4,5,9,51-67</sup>

157 The sorting depth for polygons and thickness of weathered rock at study sites were  
158 determined using electrical resistivity tomography. Soundings were carried out across the  
159 given polygon assemblage between the nearest edges of the given summit flat. The method  
160 was applied at multiple four-electrode arrays with 2-m spacing between the electrodes using  
161 the Wenner-Schlumberger measuring method.<sup>68</sup> The obtained apparent resistivity data were  
162 subjected to the geophysical inversion procedure (L1-norm) in RES2DINV software  
163 (Geotomo, Malaysia).

164 We sampled six boulders per site to increase the possibility of deriving a robust <sup>10</sup>Be  
165 chronology. At each site, we collected samples from two to three individual sorted polygons.  
166 The samples were collected preferentially from the largest upright boulders located in a  
167 border of a sampled undisturbed polygon. This approach limits the possibility of the tilting of  
168 boulders after their active upfreezing/frost heaving and reduces the effects of snow and  
169 vegetation cover.<sup>69</sup> The samples were collected using a chisel and a hammer; the samples  
170 were taken from the sampled surface to the depth of 2 to 7 cm. The dip/orientation of the  
171 sampled surfaces was measured with a clinometer and a compass and their location/altitude  
172 was determined with GPS. The characteristics of sampled boulders and study sites are given  
173 in Table 1 and 2, respectively.

### 174 3.2 <sup>10</sup>Be methodology

175 The samples were crushed, sieved and cleaned with a mixture of HCl and H<sub>2</sub>SiF<sub>6</sub>. The  
176 extraction method for <sup>10</sup>Be<sup>70, 71</sup> involves isolation and purification of quartz and elimination of  
177 atmospheric <sup>10</sup>Be. A weighed amount (~0.1 g) of a 3025 ppm solution of <sup>9</sup>Be was added to the  
178 decontaminated quartz. Beryllium was subsequently separated from the solution by successive  
179 anionic and cationic resin extraction and precipitation. The final precipitates were dried and  
180 heated at 800 °C to obtain BeO, and finally mixed with niobium powder prior to the  
181 measurements, which were performed at the French Accelerator Mass Spectrometry (AMS)  
182 National Facility ASTER (CEREGE, Aix en Provence).

183 The beryllium data were calibrated directly against the STD-11 beryllium standard using a  
184 <sup>10</sup>Be/<sup>9</sup>Be ratio of  $1.191 \pm 0.013 \cdot 10^{-11}$ .<sup>72</sup> Age uncertainties include an external AMS  
185 uncertainty of 0.5%,<sup>73</sup> blank correction and 1σ uncertainties. The <sup>10</sup>Be/<sup>9</sup>Be measured blank  
186 ratio associated to the samples presented in this paper is  $3.618 \cdot 10^{-15}$ . A density of 2.5 g cm<sup>-3</sup>  
187 was used for all samples. A sea-level, high-latitude spallation production of  $4.01 \pm 0.18$  at g<sup>-</sup>  
188 <sup>1</sup>·yr<sup>-1</sup><sup>74</sup> was used and scaled for latitude and elevation using Stone<sup>75</sup> scaling scheme. The

189 surface production rates were also corrected for the local slope and topographic shielding due  
 190 to the surrounding terrain.<sup>76</sup> Shielding from snow was estimated using an average snow  
 191 density of 0.3 g·cm<sup>-3</sup> and an estimated snow thickness and duration at sample sites.<sup>77</sup> These  
 192 values were derived from the mean thickness and duration of snow cover during the years  
 193 1961–1990 at 14 weather stations (445–1410 m a.s.l.) in the Sudetes Mountains. As the snow  
 194 cover is unevenly distributed and its variation since the exposure of sampled surfaces is  
 195 unknown, the real effect of snow shielding remains uncertain. However, most of samples  
 196 were extracted from windswept sites without vegetation and we therefore suspect that  
 197 temporal variation in snowfall has had a minor effect on snow conditions at these sites.

198 <sup>10</sup>Be concentrations were modelled using the equation:

$$C_{(x,\varepsilon,t)} = \frac{P_{spall.}}{\frac{\varepsilon}{\Lambda_n} + \lambda} \cdot e^{-\frac{x}{\Lambda_n}} \left[ 1 - \exp \left\{ -t \left( \frac{\varepsilon}{\Lambda_n} + \lambda \right) \right\} \right] + \frac{P_\mu}{\frac{\varepsilon}{\Lambda_\mu} + \lambda} \cdot e^{-\frac{x}{\Lambda_\mu}} \left[ 1 - \exp \left\{ -t \left( \frac{\varepsilon}{\Lambda_\mu} + \lambda \right) \right\} \right]$$

199

200

(1)

201 where  $C_{(x,\varepsilon,t)}$  is the nuclide concentration as a function of depth  $x$  (g·cm<sup>-2</sup>),  $\varepsilon$  the denudation  
 202 rate (g·cm<sup>-2</sup>·yr<sup>-1</sup>),  $t$  the exposure time (yr) and  $\lambda$  the radioactive decay constant (yr<sup>-1</sup>).  $P_{spall}$   
 203 and  $P_\mu$  are the relative production rates due to neutrons and muons, respectively.  $\Lambda_n$  and  $\Lambda_\mu$   
 204 are the effective apparent attenuation lengths (g·cm<sup>-2</sup>), for neutrons and muons, respectively.  
 205 The muon scheme follows Braucher et al.<sup>78</sup>

206 To estimate minimum exposure ages, denudation was set to zero whereas the exposure time  
 207 was supposed to be infinite to infer maximum denudation rates. In that latter case, it is  
 208 possible estimating the time (integration time, noted  $T_{int.}$ ) needed to reach the steady state  
 209 concentration using a modified equation based on the approach of Lal<sup>79</sup> which do not consider  
 210 muon contributions; the modified equation is:

$$T_{int.} = \frac{\%P_{spall}}{\frac{Ln(2)}{1387000} + \frac{\varepsilon}{160}} + \frac{\%P_{\mu Slow}}{\frac{Ln(2)}{1387000} + \frac{\varepsilon}{1500}} + \frac{\%P_{\mu Fast}}{\frac{LN(2)}{1387000} + \frac{\varepsilon}{4320}}$$

211

(2)



212 where %*P<sub>spall</sub>*, %*P<sub>μSlow</sub>* and %*P<sub>μFast</sub>* are the percentage contributions of neutrons, Slow  
213 and Fast muons respectively in the total production and 160, 1500 and 4320 g.cm<sup>-2</sup> their  
214 respective attenuation lengths.

### 215 3.3 Data treatment

216 We assess the distribution of exposure ages obtained at individual sample sites, compare the  
217 arithmetic means and standard deviations calculated for four age populations, and interpret the  
218 chronological data with exposure ages reported from the Sudetes Mountains in previous  
219 studies.

220 We first analyse the scatter in exposure-age data sets for each sample site because the age  
221 distribution reflects the exposure history of sampled surfaces and indicates main sources of  
222 geological uncertainties - cosmogenic-nuclide inheritance and disturbance of boulders after  
223 emplacement.<sup>80</sup> Among a group of sample, a sample with inherited <sup>10</sup>Be can be identified by a  
224 higher concentration yielding to older age than the mean of the remaining ages. By contrast, a  
225 significant younger age may indicate incomplete exposure of the sampled boulder. The  
226 distribution of the exposure ages obtained for the given sample site and scatter in the age  
227 groups were approximated using the reduced chi-square statistics ( $\chi_R^2$ ) and a standard  
228 deviation (SD) to the arithmetic mean exposure age ratio. Following the procedure presented  
229 by Blomdin et al.,<sup>81</sup> age groups that have  $\chi_R^2 \leq 2$  are classified as well-clustered, groups that  
230 show  $\chi_R^2 > 2$  but SD  $\leq 15\%$  of the mean exposure age are considered as moderately-clustered,  
231 and groups that show  $\chi_R^2 > 2$  and SD  $> 15\%$  of the mean age are designated as poorly-  
232 clustered.

**Commentaire [Régis2]:** In table 2 a class cluster is still present ( Class C) Is it normal?

233 Subsequently, we calculated an arithmetic mean and standard deviations (1s) for each site,  
234 compare these values, and assessed their relevance for regional estimate of polygon  
235 chronology. When the age ranges of two or more sample sites overlap within their analytical  
236 uncertainties we consider them representative as a regional interval of the sorted polygon  
237 formation. We compare this interval with regional glaciation chronology and we interpret the  
238 data with respect to exposure ages reported for periglacial landforms in the Sudetes  
239 Mountains.<sup>82, 83</sup> An apparent age that differs significantly from the resulting age range is  
240 excluded from chronological consideration. A number of factors can cause apparent exposure  
241 ages of the sampled landforms and these are discussed in section 5.1.

242

## 243 **4 Results**

### 244 *4.1 Morphology of sorted polygons*

245 The sorted polygons occur on flat or gently inclined surfaces (Fig. 2bcde, 3bcde) with the  
246 median slope around 3° (Table 2). The length and width of the polygons range between 2.5–  
247 10.5 m and 2.1–6.4 m, respectively (Table 3). The sorted polygons on Vysoké Kolo (VK)  
248 have the largest average length (6.97 m), followed by the polygons on Břidličná hora (BR)  
249 and Větrná louka (VL), while the patterns with the smallest average length (3.67 m) lie on  
250 Luční hora (LH). The polygons on Luční hora have significantly smaller width (Fig. 5) than  
251 the polygons at other study sites (i.e. LH vs VK:  $F(1.41) = 26.643$ ,  $p = 0.00001$ ; LH vs BR:  
252  $F(1.62) = 19.491$ ,  $p = 0.00004$ ; LH vs VL:  $F(1.38) = 14.576$ ,  $p = 0.00048$ ). The sorted  
253 polygons with the largest average height lie on Větrná louka (Table 3, Fig. 5), which  
254 significantly differs from other study sites (i.e. VL vs LH:  $F(1.38) = 260.24$ ;  $p < 0.00001$  VL  
255 vs VK:  $F(1.17) = 71.698$ ,  $p < 0.00001$ ; VL vs BR:  $F(1.38) = 201.41$ ;  $p < 0.00001$ ).

### 256 *4.2 Regolith thickness*

257 The high electrical-resistivity zones of more than ca. 60,000  $\Omega \cdot \text{m}$  at the Vysoké Kolo, Luční  
258 hora, and Břidličná hora sites (Fig. 6a, 6b and 6c) are associated with the presence of air-filled  
259 debris. By contrast, the resistivity of the weathering mantle at Větrná louka is lower (Fig. 6d)  
260 because this site lies below the alpine timberline and is covered with a thick top soil layer,  
261 which supports the cavities between the boulders with fine-grained materials. In addition, the  
262 quartzite vein crossing the Větrná louka site causes a slight bedrock protrusion, while at other  
263 locations the bedrock is mostly parallel to the ground surface. The regolith at the Vysoké  
264 Kolo, Břidličná hora, and Větrná louka sites is two to three times thicker than on Luční hora  
265 where regolith/bedrock transition is around 2 m (Fig. 6b) below the ground surface. The small  
266 depth of bedrock at this site is constrained by the nearest cryoplanation terrace located 3 m  
267 lower.

### 268 *4.3 Exposure ages*

269 For all studied sites, surface exposure age are scattered (Table 1) and age groups are poorly  
270 clustered (Table 2). Exposure ages obtained for the patterned ground on Vysoké Kolo yield a  
271 mean age of  $25.4 \pm 1.9$  ka and an oldest age of  $30.3 \pm 1.1$  ka. This boulder group has the  
272 smallest scatter and ages range from 19 to 30 ka. Boulder group from the sorted polygons on  
273 Luční hora have a mean age of  $53.6 \pm 11.4$  ka. The exposure ages from this summit flat show

274 the largest scatter of all the study sites, ranging from  $91.3 \pm 2.8$  ka to  $9.0 \pm 5.6$  ka. Exposure  
275 ages obtained on Břidličná hora yield a mean age of  $28.0 \pm 1.0$  ka and a maximum age of  $38.1$   
276  $\pm 1.6$  ka. This oldest age is significantly older than the calculated mean age but remaining  
277 ages fall within a narrow range of 23–29 ka. Boulder group from Větrná has a mean exposure  
278 age of  $24.3 \pm 4.8$  ka and an oldest age of  $47.9 \pm 1.4$  ka that is an obvious outlier according to  
279 the  $\chi^2$  criterion.

#### 280 *4.4 Steady-state denudation rates*

281 Considering the possibility that all samples have reached the denudational steady state (time  
282 being considered as infinite in eq. 1), the measured  $^{10}\text{Be}$  concentrations may help to estimate  
283 maximum steady state denudation rates. The highest values were obtained for the Větrná  
284 louka site where all but one (VL2) samples yield maximum steady state denudation rates  
285 ranging from 30 to 43 mm/ka. The denudation rate of  $79.3 \pm 49.4$  mm/ka was calculated for  
286 the sample LH4 but large uncertainty precludes robust interpretation of this value. Moreover,  
287 other samples from the Luční hora site yield lower denudation rates than samples collected at  
288 the remaining study sites (Table 1).

## 289 **5 Discussion**

### 290 *5.1 Exposure age interpretation and uncertainties*

291 The scatter in age groups indicates that some sampled boulders experienced complex  
292 exposure history or post-exposure disturbance. An observed distribution of six exposure ages  
293 is affected by the presence of one or two underestimated ages and one overestimated age at all  
294 but one sample site. A significantly older sample age than the mean exposure age calculated  
295 for the landform results from cosmogenic-nuclide inheritance.<sup>84</sup> The most probable reason for  
296 inherited nuclide concentration in boulders that form the margins of sorted polygons is their  
297 initial position at shallow subsurface depth affected by cosmic-ray flux. The cosmogenic-  
298 nuclide production decreases rapidly with depth and it is largely attenuated below ~1 m  
299 depth.<sup>85</sup> Boulders located below fine-grained regolith in this thin subsurface zone (Fig. 8B)  
300 contain inherited  $^{10}\text{Be}$  from a period prior to the frost-heave event and they will show  
301 apparently older age than boulders with zero inherited nuclide concentration frost-heaved  
302 from greater depths. An alternative scenario that could lead to inheritance deals with the  
303 repeated phase of polygon formation and emplacement of boulders that had experienced  
304 previous exposure at the margins of former polygons. However, this scenario is less probable

305 as most of these boulders disintegrate over the period between two subsequent cold stages and  
306 similar or higher freeze-thaw activity would be necessary to rearrange existing polygons.

307 The presence of apparently younger boulders in the margins of sorted polygon could be  
308 attributed to post-exposure tilting of sampled surfaces<sup>87</sup> rather than to surface erosion or  
309 disintegration because only boulders without signs of erosion or fractures were sampled. The  
310 post-exposure shielding of sample sites by ice or snow cover can be excluded from this  
311 consideration too. Glaciers were confined to cirques and valleys during the LGM<sup>82</sup> and  
312 hypothetical plateau ice fields were suggested to cover high elevations except for wind-swept  
313 top of the ridges.<sup>88</sup> The presence of permanent snow cover is rather improbable because of  
314 reduced precipitation (25–75%) in cold stages<sup>37, 89</sup> and more effective deflation by enhanced  
315 winds.<sup>36</sup> Finally, the younger age of particular boulders cannot result from mass-shielding by  
316 vegetation and/or soil cover that is evenly spread over the sample sites.

317 The obtained chronological data suggest that the large sorted polygons in the Sudetes  
318 Mountains developed during the last glacial period. Considering relatively small areal extent  
319 of the Sudetes Mountains, narrow elevation range of sample sites, and similar topographic and  
320 climate conditions at these sites, the period of formation of large sorted polygons could have  
321 occurred around the same time throughout the Sudetes. However, the summed probability  
322 density distribution of the obtained <sup>10</sup>Be exposure ages is bimodal with a main peak centred  
323 on 25 ka and a minor increase around 64 ka (Fig. 7, black curve). The main peak indicates  
324 that the formation of sorted polygon started no later than 30 ka, reached a climax around 25  
325 ka, and ceased after 18 ka. The second modelled peak reflects high levels of *in situ* produced  
326 <sup>10</sup>Be in samples from the Luční hora site. These samples seem to be affected by inheritance as  
327 indicated by apparently older mean age ( $53.6 \pm 11.4$  ka) compared to other sites ( $24.3 \pm 4.8$  ka  
328 to  $27.9 \pm 2.3$  ka). The possible reasons for the inheritance are discussed below. The reduced  
329 dataset ( $n = 18$ ) without exposure ages from Luční hora yields the mean exposure age of  $25.0$   
330  $\pm 0.4$  ka (Fig. 7, grey curve).

331 The largest scatter in the age group from Luční hora confirms that inheritance must be  
332 considered at this site. The exposure age of  $91.3 \pm 2.8$  ka is the oldest within the whole  
333 dataset, and the apparent mean age is significantly older than the timing of the established  
334 main phase of polygon formation. The inheritance at this site may be tentatively attributed to  
335 the quartzite bedrock and poorly developed regolith cover. Despite the presence of surface  
336 features caused by differential weathering, the quartzite is more resistant to physical

337 weathering and erosion than granite and phyllite at other sample sites. The hardness of the  
338 massive quartzite and considerably reduced surface lowering of landforms built by this rock  
339 were reported from many regions including the Sudetes Mountains.<sup>32, 90</sup> The effect of the rock  
340 hardness on an exposure age was observed by Guido et al.,<sup>91</sup> who reported a significantly  
341 older exposure age (30.1 ka) for a quartzite knoll compared to ages from other rock types  
342 (12.3 to 17.1 ka).

343 The hardness of the quartzite exerts control on the rate of weathering that is much lower  
344 compared to weathering rate of granite and phyllite bedrock. As a result, a thin layer of  
345 regolith has formed on Luční hora where bedrock lies only around 2 m below the ground  
346 surface. By contrast, 4 to 9 m of weathered rock cover the bedrock at the remaining study  
347 sites (Fig. 6). The sorting depth corresponds with the thickness of regolith cover ranging from  
348 less than 0.5 m on Luční hora to around 1.4 m on Břidličná hora.<sup>92, 93</sup> Considering the mean  
349 attenuation path length of neutrons in rocks<sup>84</sup> and the depth of boulders (>0.5 m) before the  
350 initiation of polygon formation on Luční hora, the relatively small boulders at this site contain  
351 a substantial inherited nuclide component. By contrast, larger boulders that form polygons at  
352 other sites (Table 2) have significantly less inherited <sup>10</sup>Be as these were frost heaved from the  
353 depth of more than 1.4 m.

354 The high fraction of boulder ages with inheritance indicate that exposure dating should be  
355 applied on polygon boulders with caution. The age uncertainty resulting from the effects of  
356 vegetation and snow cover shielding seems to be of minor importance. All sample sites except  
357 Větrná louka are located above the timberline in the zone of limited vegetation and snow  
358 cover that is effectively transported from the summit flats by the prevailing westerly winds.<sup>42</sup>  
359 The timberline increased to its current position in the Sudetes Mountains during the early  
360 Holocene, and forest has covered Větrná louka site at least over the last 8 ka.<sup>94</sup> Considering  
361 that boreal forest can reduce the cosmic ray flux by  $2.3 \pm 0.6\%$ ,<sup>95</sup> the estimated timing of  
362 polygons at this site could be underestimated only by a few hundred years.

### 363 *5.2 Paleoenvironmental implications*

364 The exposure ages indicate that large sorted polygons in the Sudetes Mountains formed  
365 during the Upper Pleniglacial (34.8–14.7 ka)<sup>96</sup> after a period of unstable climate in the second  
366 part of MIS 3.<sup>97, 98</sup> The onset of the polygon formation corresponds to the Greenland sub-  
367 stadal GS-5.1 (30.6–28.9 ka)<sup>99</sup> and the main activity of these landforms reflects extremely  
368 cold and relatively wet conditions in the Northern Hemisphere during the stadal GS-3 (27.5–

369 23.3 ka).<sup>100</sup> The period of polygon formation overlaps with the range of 30–24 ka (Fig. 9),  
370 which is considered as the period of the maximum extension of permafrost (Last Permafrost  
371 Maximum, LPM)<sup>111</sup> in Western Europe during the last glacial cycle.<sup>102</sup> The timing of the  
372 dated polygons is in line with the two (35–31 and 22–20 ka) out of four main phases of  
373 periglacial activity in Britain lowlands,<sup>22</sup> and corresponds to some phases ( $30.0 \pm 2.5$ ,  $24.0 \pm$   
374  $1.1$  and  $20.7 \pm 0.7$  ka) of ice-wedge activity in France.<sup>102</sup>

375 The onset of differential frost heave in the Sudetes coincides with the pre-LGM period of  
376 periglacial conditions indicated recently by <sup>10</sup>Be exposure ages (Fig. 9). The exposure age of  
377  $36.5 \pm 2.1$  ka and  $29.7 \pm 2.1$  ka reported for a summit tor and ploughing block, respectively,  
378 delimit the interval of bedrock disintegration and enhanced solifluction in the Krkonoše  
379 Mountains (Fig. 9).<sup>82</sup> Four exposure ages ( $84.3 \pm 3.8$  to  $26.8 \pm 2.6$  ka) retrieved recently for a  
380 block slope adjacent to the Větrná louka site constrain the pre-LGM timing of cold  
381 environments in the Hrubý Jeseník Mountains.<sup>83</sup> At that time, permafrost reached its  
382 maximum extent and thickness (220–250 m) as indicated by the subsurface post-cryogenic  
383 structures near the eastern boundary of the Sudetes Mountains,<sup>112</sup> the model-based estimates<sup>36</sup>  
384 and the cryogenic cave carbonates.<sup>113</sup> The size of polygons dated in this study implies active-  
385 layer thickness of 0.9–1.6 m. This range is consistent with the summer thawing to the depth of  
386 1 m suggested by Jahn<sup>114</sup> for LGM interval.

387 The occurrence of sorted polygons indicates cold conditions and lack of thick snow cover on  
388 the upper slopes of the Sudetes Mountains between 30 and 18 ka. Considering the most  
389 respected temperature threshold for the sorted polygon formation, the MAAT was lower than  
390  $-4$  °C.<sup>9</sup> The derived palaeotemperature represents maximal value for elevation range of 1210–  
391 1270 m a.s.l. where dated polygons are preserved at Větrná louka site. Assuming the near-  
392 surface lapse rate in the lower troposphere (0.65 K/100 m), the MAAT on the summit flats  
393 around 1550 m a.s.l. was probably lower than  $-6$  °C. The estimated temperature range is  
394 higher than the MAAT estimates for LGM that vary between  $-8$  and  $-10$  °C.<sup>37, 115</sup> However,  
395 the palaeotemperatures derived in this study must be regarded as maximal thresholds only  
396 because sorted polygons are also found at lower elevations within the Sudetes Mountains.

397 Regional amelioration of the climate after around 18 ka<sup>101</sup> led to the gradual degradation of  
398 permafrost in the Sudetes Mountains.<sup>36</sup> The intensity of frost action decreased allowing only  
399 for cryoturbation, solifluction and limited sorting of fine-grained covers.<sup>116</sup> The periglacial  
400 activity increased again at the end of the Lateglacial period when the climate cooled and

401 permafrost re-aggraded.<sup>101, 117</sup> The exposure ages reported for moraines ( $13.5 \pm 0.5$  to  $12.9 \pm$   
402  $0.7$  ka) and pronival ramparts ( $13.8 \pm 0.4$  ka) in the Krkonoše Mountains indicate glacier re-  
403 advance and enhanced frost action (Fig. 9).<sup>82</sup> At that time, frost sorting and solifluction were  
404 probably reactivated.<sup>117</sup> Small sorted patterns observed in the large dated polygons on Luční  
405 hora summit flat may be tentatively attributed to that period though their later formation  
406 cannot be excluded.<sup>49</sup> During the Holocene, the frost action has been limited to cryoturbation,  
407 solifluction and sorting of sandy covers in deflation areas with thin snow cover.<sup>50</sup>

### 408 *5.3 Summit flat denudation*

409 The observed differences in the maximum steady state denudation rates between the sample  
410 sites may reflect varying topography and bedrock conditions that control the intensity of  
411 surface processes on summit planation surfaces. The denudation rates  $<20$  mm/ka obtained  
412 for the Luční hora site represent the highest summit planation surface in the Sudetes  
413 Mountains underlain by quartzite (Table 2). Well-preserved morphology and small elongation  
414 of the sorted polygons on this near-horizontal site indicate low rate of weathering and slope  
415 processes. Higher values of denudation rates inferred for Vysoké Kolo and Břidličná hora are  
416 consistent with less resistant bedrock (granite and phyllite) and more intense surface transport.  
417 The latter assumption is supported by the lower values of width/length index calculated for  
418 the preserved sorted polygons (Table 3). The highest denudation rates ( $\sim 40$  mm/ka) were  
419 obtained for the Větrná louka site, which represents a lowered planation surface on a side  
420 ridge build by phyllites.

421 The observed denudation rates are comparable to the values derived from cosmogenic  
422 nuclides for bedrock outcrops in mid-latitude mountain regions. The low values determined  
423 for the highest planation surface in the Krkonoše Mountains correspond with the denudation  
424 rates reported for summit flats in Western U.S. mountain ranges ( $2\text{--}19$  mm/ka),<sup>119</sup> ridgeline  
425 outcrops in the Appalachian Mountains ( $\sim 9$  mm/ka),<sup>120</sup> and arête-shaped ridges in the  
426 Pyrenees ( $9\text{--}21$  mm/ka).<sup>121</sup> The higher intensity of denudation determined for the lower  
427 planation surfaces in the Sudetes ranges is in line with the denudation rates reported for  
428 bedrock outcrops in the Rocky Mountains ( $22\text{--}45$  mm/ka)<sup>122, 123</sup> and flat ridges in the  
429 Pyrenees ( $30\text{--}40$  mm/ka).<sup>121</sup> This rate is also consistent with the catchment-wide denudation  
430 values derived from cosmogenic nuclides in the Vltava River terrace sequences south from  
431 the Sudetes Mountains ( $23\text{--}31$  mm/ka).<sup>124</sup>

432 The maximum steady state denudation rates determined from  $^{10}\text{Be}$  concentrations for the  
433 high-elevated sites provide new insights into the planation history of the Sudetes Mountains.  
434 Until now, the intensity of denudation was inferred only for time scales of  $10^7$  to  $10^8$  years  
435 based on the thermochronological data and sedimentary record. Three periods of accelerated  
436 denudation were suggested for the Sudetes over its post-Variscan history with the denudation  
437 rates as high as 300 m/Ma during the early Permian, Early Triassic and Late Cretaceous.<sup>125</sup>  
438 Significantly lower rates ranging from ~16 to <0.1 mm/ka with the mean of ~7 mm/ka were  
439 derived for the post-75 Ma period.<sup>46</sup> However, the long-term denudation rates provide little  
440 evidence of surface lowering under glacial and interglacial conditions in the Quaternary. Our  
441 data indicate denudation rates on the order of tens of mm/ka during the last glacial period.  
442 This suggests that the intensity of denudation increased during the Quaternary compared to  
443 Paleogene and Neogene periods.<sup>126</sup>

## 444 **6 Conclusions**

445 Surface exposure dating using cosmogenic  $^{10}\text{Be}$  provides the first geochronological data for  
446 the sorted forms of patterned ground in central Europe.  $^{10}\text{Be}$  exposure ages from the large  
447 sorted polygons at four sites in the Sudetes Mountains imply that these periglacial features  
448 started to form no later than 30 ka and their activity decreased after 20 ka. The initiation of  
449 polygon formation is consistent with the most widespread events of thermal-contraction  
450 cracking during the LPM in central Europe, and with periods of enhanced periglacial activity  
451 in lowland Britain and France. The main phase of formation falls within the global LGM,  
452 matches the period of maximum glaciation and continuous permafrost distribution in  
453 European mountains, and correlates with the period of intense periglacial activity in the  
454 surrounding lowland areas.

455 The maximum steady state denudation rates calculated for the sample sites are on the order of  
456 tens of mm/ka and corresponding integration times on the order of  $10^4$  years. The observed  
457 denudation rates are comparable to those reported from summit flats and ridgeline outcrops in  
458 mid-latitude mountain regions and they constrain regional estimates for the temporal  
459 variability of the denudation.

460 The samples collected from the sorted polygons provide large scatter in exposure ages and  
461 significant age uncertainty. This scatter may result from the incorporation of boulders that are  
462 affected by inheritance or disturbances after their active upfreezing/frost heaving. The  
463 morphological evaluation of individual polygons and their assemblages at the study site is



464 highly advisable as its results would allow for sample collections from suitable boulders and  
465 landforms. Although this evaluation reduces the possibility of sampling eroded or disturbed  
466 polygon, the complex history of earlier exposure and/or later reactivation cannot be fully  
467 excluded.

#### 468 **Acknowledgements**

469 The research was supported by the Czech Science Foundation (project no. 17-21612S). The  
470 Administrations of the Krkonoše Mountains National Park and the Protected Landscape Area  
471 of Jeseníky are acknowledged for providing permissions to work in the protected areas.  
472 ASTER AMS national facility (CEREGE, Aix-en-Provence) is supported by the  
473 INSU/CNRS, the ANR through the "Projets thématiques d'excellence" program for the  
474 "Equipements d'excellence" ASTER-CEREGE action, IRD. The data that support the  
475 findings of this study are available from the corresponding author upon reasonable request.  
476 The authors are grateful for helpful and constructive comments from two anonymous referees.

#### 477 **References**

- 478 1. Hallet B. Stone circles: form and soil kinematics. *Philos T R Soc A*,  
479 2013;**371**:20120357.
- 480 2. Ballantyne CK. Patterned ground. In: Elias SA, Mock CJ, eds. *Encyclopedia of*  
481 *Quaternary Science*. 2<sup>nd</sup> ed. Amsterdam: Elsevier; 2013:452–463.
- 482 3. Harris SA, Brouchkov A, Guodong C. Geocryology: *Characteristics and Use of Frozen*  
483 *Ground and Permafrost Landforms*. London: CRC Press; 2018.
- 484 4. Grab S. Characteristics and paleoenvironmental significance of relict sorted patterned  
485 ground, Drakensberg plateau, Southern Africa. *Quaternary Sci Rev*. 2002;**21**:1729–  
486 1744.
- 487 5. Uxa T, Mida P, Křížek M. The effect of climate on Morphology and Development of  
488 sorted circles and polygons. *Permafrost Periglac*. 2017;**28**:663–674.
- 489 6. Winkler S, Matthews JA, Mourné RW, Wilson P. Schmidt-hammer exposure ages from  
490 periglacial patterned ground (sorted circles) in Jotunheimen, Norway, and their  
491 interpretative problems. *Geogr Ann A*. 2016;**98**:265–285.
- 492 7. Matsuoka N. Climate and material controls on periglacial soil processes: towards  
493 improving periglacial climate indicators. *Quat Res*. 2011;**75**:356–365.
- 494 8. Goldthwait RP. Frost Sorted Patterned Ground: A Review. *Quat Res*. 1976;**6**:27–35.
- 495 9. D'Amico ME, Pintaldi E, Catoni M, Freppaz M, Bonifacio E. Pleistocene periglacial  
496 imprinting on polygenetic soils and paleosols in the SW Italian Alps. *Catena*.  
497 2019;**174**:269–284.
- 498 10. Van Vliet-Lanoë B. Patterned ground and climate change. In: Pokrovsky OS, ed.  
499 *Permafrost: distribution, composition and impacts on infrastructure and ecosystems*.  
500 New York, NY: Nova Science Publishers; 2014:67–106.

- 501 11. Matsuoka N, Abe M, Ijiri M. Differential frost heave and sorted patterned ground: Field  
502 measurements and a laboratory experiment. *Geomorphology*. 2003;**52**:73–85.
- 503 12. Peterson RA, Krantz WB. Differential frost heave model for patterned ground  
504 formation: Corroboration with observations along a North American arctic transect. *J*  
505 *Geophys Res-Biogeophys*. 2008;**113**:G03S04.
- 506 13. Kessler MA, Werner BT. Self-organization of sorted patterned ground. *Science*.  
507 2003;**299**:380–383.
- 508 14. Van Vliet-Lanoë B, Seppälä M. Stratigraphy, age and formation of peaty earth  
509 hummocks (pounus), Finnish Lapland. *Holocene*. 2002;**12**:187–199.
- 510 15. Kling J. Relict sorted patterned ground in Rostu, Northernmost Sweden. *Geogr Ann A*.  
511 1996;**78**:61–72.
- 512 16. Jeong G. Radiocarbon ages of sorted circles on King George Island, South Shetland  
513 Islands, West Antarctica. *Antarct Sci*. 2006;**18**:265–270.
- 514 17. Kelly M, Denton G, Hall B. Late Cenozoic paleoenvironment in southern Victoria  
515 Land, Antarctica, based on a polar glaciolacustrine deposit in western Victoria Valley.  
516 *Geol Soc Am Bull*. 2002;**114**:605–618.
- 517 18. Bateman MD. Thermoluminescence dating of the British coversand deposits.  
518 *Quaternary Sci Rev*. 1995;**14**:791–798.
- 519 19. Bateman MD, Hitchens S, Murton JB, Lee JR, Gibbard PL. The evolution of periglacial  
520 patterned ground in East Anglia, UK. *J Quaternary Sci*. 2014;**29**:301–317.
- 521 20. Fábíán SÁ, Kovács J, Varga G, et al. Distribution of relict permafrost features in the  
522 Pannonian Basin, Hungary. *Boreas*. 2014;**43**:722–732.
- 523 21. Rittenour TM. Dates and Rates of Earth-Surface Processes Revealed using  
524 Luminescence Dating. *Elements*. 2018;**14**:21–26.
- 525 22. Bateman MD. Luminescence dating of periglacial sediments and structures. *Boreas*.  
526 2008;**37**:574–588.
- 527 23. Marchant DR, Lewis AR, Phillips WM, et al. Formation of patterned ground and  
528 sublimation till over Miocene glacier ice in Beacon Valley, southern Victoria Land,  
529 Antarctica. *Geol Soc Am Bull*. 2002;**114**:718–730.
- 530 24. Levy J, Marchant D, Head J. Distribution and origin of patterned ground on Mullins  
531 Valley debris-covered glacier, Antarctica: The roles of ice flow and sublimation.  
532 *Antarct Sci*. 2006;**18**:385–397.
- 533 25. Winkler S, Matthews JA, Haselberger S, Hill JL, Mourne RW, Owen G, Wolson P.  
534 Schmidt-hammer exposure-age dating (SHD) of sorted stripes on Juvflye, Jotunheimen

- 535 (central South Norway): Morphodynamic and palaeoclimatic implications.  
536 *Geomorphology*. 2020;**353**:107014.
- 537 26. Ballantyne CK, Stone JO. Trimlines, blockfields and the vertical extent of the last ice  
538 sheet in southern Ireland. *Boreas*. 2015;**44**:277–287.
- 539 27. Andrés N, Gómez-Ortiz A, Fernández-Fernández JM, et al. Timing of deglaciation and  
540 rock glacier origin in the southeastern Pyrenees: a review and new data. *Boreas*.  
541 2018;**47**:1050–1071.
- 542 28. Denn AR, Bierman PR, Zimmemrman SRH, Caffee MW, Corbett LB, Kirby E.  
543 Cosmogenic nuclides indicate that boulder fields are dynamic, ancient,  
544 multigenerational features. *GSA Today*. 2018;**28**:4–10.
- 545 29. Migoń P, Lidmar-Bergström K. Weathering mantles and their significance for  
546 geomorphological evolution of central and northern Europe since the Mesozoic. *Earth*  
547 *Sci Rev*. 2001;**56**(1–4):285–324.
- 548 30. Högbom B. Über die geologische Bedeutung des Frostes. *Bull Geol Inst*. 1914;**12**:257–  
549 390.
- 550 31. Sekyra J, Kociánová M, Štursová H, Dvořák IJ, Svoboda M. Frost phenomena in  
551 relationship to mountain pine. *Opera Corcon*. 2002;**39**:69–114.
- 552 32. Traczyk A, Migoń P. Cold-climate landform patterns in the Sudetes. Effect of lithology,  
553 relief and glacial history. *Acta U Carol Geogr Suppl*. 2000;**35**:185–210.
- 554 33. Tremel V, Migoń P. Controlling factors limiting timberline position and shifts in the  
555 Sudetes: A review. *Geogr Pol*. 2015;**88**:55–70.
- 556 34. Ehlers J, Gibbard PL, Hughes PD, eds. *Quaternary Glaciations - Extent and*  
557 *Chronology: A Closer Look*. Amsterdam: Elsevier; 2011.
- 558 35. Antoine P, Rousseau DR, Degeai JP, et al. High-resolution record of the environmental  
559 response to climatic variations during the last interglacial-glacial cycle in Central  
560 Europe: The loess-palaeosol sequence of Dolní Věstonice (Czech Republic).  
561 *Quaternary Sci Rev*. 2013;**67**:17–38.
- 562 36. Czudek T. *Vývoj relief České republiky v kvartéru*. Brno: Moravské zemské museum;  
563 2005.
- 564 37. Heyman BM, Heyman J, Fickert T, Harbor JM. Paleo-climate of the central European  
565 uplands during the last glacial maximum based on glacier mass-balance modeling.  
566 *Quaternary Res*. 2013;**79**:49–54.

- 567 38. Nývlt D, Engel Z, Tyráček J. Pleistocene glaciations of Czechia. In: Ehlers J, Gibbard  
568 PL, Hughes PD, eds. *Quaternary Glaciations - Extent and Chronology: A Closer Look*.  
569 Amsterdam: Elsevier; 2011:37–46.
- 570 39. Halášová O, Hančarová E, Vašková I. Časová a prostorová variabilita vybraných  
571 klimatologických a hydrologických prvků na území Krkonoš za období 1961-2000.  
572 *Opera Corcon*. 2007;**44**:171–178.
- 573 40. Daniel M, Materna J, Honig V, et al. Vertical Distribution of the Tick *Ixodes ricinus*  
574 and Tick-borne Pathogens in the Northern Moravian Mountains Correlated with Climate  
575 Warming (Jeseníky Mts., Czech Republic). *Cent Eur J Publ Heal*. 2009;**17**:139–145.
- 576 41. Coufal L, Míková T, Langová P. *Meteorologická data na území ČR za období 1961–90*.  
577 Praha: Český hydrometeorologický ústav; 1992.
- 578 42. Spusta V, Spusta V, Kociánová M. Ukládání sněhu na závětrných svazích české strany  
579 Krkonoš (tundrová zóna). *Opera Corcon*. 2003;**40**:87–104.
- 580 43. Žák J, Verner K, Sláma J, Kachlík V, Chlupáčová M. Multistage magma emplacement  
581 and progressive strain accumulation in the shallow-level Krkonoše-Jizera plutonic  
582 complex, Bohemian Massif. *Tectonics*. 2013;**32**:1493–1512.
- 583 44. Placek A, Migoń P, Żyszkowska W. Low-gradient surfaces in the Sudetes – insights  
584 from the digital elevation model. *Univ Ostrav Acta Fac Rerum Nat Geogr Geol*.  
585 2007;**237**:94–110.
- 586 45. Křížek M, Krause D, Uxa T, Engel Z, Tremel V, Traczyk A. Patterned ground above the  
587 alpine timberline in the High Sudetes, Central Europe. *J Maps*. 2019;**15**(2):563–569.
- 588 46. Danišík M, Migoń P, Kuhlemann J, Evans NJ, Dunkl I, Frisch W. Thermochronological  
589 constraints on the long-term erosional history of the Karkonosze Mts., central Europe.  
590 *Geomorphology*. 2010;**117**:78–89.
- 591 47. Janoušek V, Aichler J, Hanžl P, et al. Constraining genesis and geotectonic setting of  
592 metavolcanic complexes: A multidisciplinary study of the Devonian Vrbno Group  
593 (Hrubý Jeseník Mts., Czech Republic). *Int J Earth Sci*. 2014;**103**:455–483.
- 594 48. Křížek M. Periglacial Landforms of the Hrubý Jeseník Mountains In: Pánek T,  
595 Hradecký J, eds. *Landscapes and Landforms of the Czech Republic*. Cham: Springer;  
596 2016:277–289.
- 597 49. Křížek M, Uxa T. Morphology, Sorting and Microclimates of Relict Sorted Polygons,  
598 Krkonoše Mountains, Czech Republic. *Permafrost Periglac*. 2013;**24**:313–321.

- 599 50. Trembl V, Křížek M, Engel Z. Classification of patterned ground based on morphology  
600 and site characteristics: a case study from the High Sudetes, Central Europe. *Permafrost*  
601 *Periglac.* 2010;**21**:67–77.
- 602 51. Ballantyne CK, Harris C. *The Periglaciation of Great Britain*. Cambridge: Cambridge  
603 University Press; 1994.
- 604 52. Ballantyne CK, Matthews JA. The Development of Sorted Circles on Recently  
605 Deglaciaded Terrain, Jotunheimen, Norway. *Arctic Alpine Res.* 1982;**14**:341–354.
- 606 53. Cook JD. *Active and relict sorted circles, Jotunheimen, Norway: a study of the*  
607 *altitudinal zonation of periglacial processes* [dissertation] Cardiff: University of Wales;  
608 1989.
- 609 54. Ellenberg L. Rezente Periglazialerscheinungen auf Cheju Dô, Südkorea. *Geogr*  
610 *Helvetica.* 1976;**31**:69–74.
- 611 55. Freund R. Die Kleinformen der Frostmusterböden: Vergleich Arktis - Alpen -  
612 Tropisches Hochgebirge. *Geogr Helvetica.* 1971;**26**:142–147.
- 613 56. Furrer G. Die Strukturformen der Alpen. *Geogr Helvetica.* 1955;**10**:193–213.
- 614 57. Gleason KJ, Krantz WB, Caine N, George JH, Gunn RD. Geometrical Aspects of  
615 Sorted Patterned Ground in Recurrently Frozen Soil. *Science.* 1986;**232**:216–220.
- 616 58. Grab SW. Annually re-forming miniature sorted patterned ground in the High  
617 Drakensberg, southern Africa. *Earth Surf Proc Land.* 1997;**22**:733–745.
- 618 59. Hallet B, Prestrud S. Dynamics of periglacial sorted circles in Western Spitsbergen.  
619 *Quaternary Res.* 1986;**26**:81–99.
- 620 60. Holness SD. Sorted circles in the maritime Subantarctic, Marion Island. *Earth Surf Proc*  
621 *Land.* 2003;**28**:337–347.
- 622 61. Humlum O, Christiansen HH. Mountain Climate and Periglacial Phenomena in the  
623 Faeroe Islands. *Permafrost Periglac.* 1998;**9**:189–211.
- 624 62. Kück KM. *Periglacial features in the vicinity of Tiffindell ski resort, North East Cape*  
625 *Drakensberg, South Africa, and their implications for the development of the resort*  
626 [dissertation]. Grahamstown: Rhodes University; 1996.
- 627 63. Ray RJ, Krantz WB, Caine TN, Gunn RD. A model for sorted patterned-ground  
628 regularity. *J Glaciol.* 1983;**29**:317–337.
- 629 64. Troll C. Strukturböden, Solifluktion und Frostklimate der Erde. *Geol Rundsch.*  
630 1944;**34**:545–694.
- 631 65. Wilson P. Small-scale Patterned Ground, Comeragh Mountains, Southeast Ireland.  
632 *Permafrost Periglac.* 1992;**3**:63–70.

- 633 66. Wilson P, Clark R. Development of Miniature Sorted Patterned Ground Following Soil  
634 Erosion in East Falkland, South Atlantic. *Earth Surf Proc Land*. 1991;**16**:369–376.
- 635 67. Love A. Patterned Ground at Beartooth Butte and East Summit, Wyoming: Geometry,  
636 Analysis, and Origin. In: Carson RJ, DeSimone D, Leonard EM, eds. *Quaternary  
637 Geology of the Clarks Fork Region, Northwestern Wyoming and Adjacent Montana*.  
638 Claremont, CA: Keck Geology Consortium; 1995:113–116.
- 639 68. Milsom J. *Field Geophysics*. Chichester: Wiley; 2003.
- 640 69. Heyman J, Applegate PJ, Blomdin R, Gribenski N, Harbor JM, Stroeven AP. Boulder  
641 height e exposure age relationships from a global glacial  $^{10}\text{Be}$  compilation. *Quat  
642 Geochronol*. 2016;**34**:1–11.
- 643 70. Chmeleff J, von Blanckenburg F, Kossert K, Jakob D. Determination of the  $^{10}\text{Be}$  half-  
644 life by multicollector ICP-MS and liquid scintillation counting. *Nucl Instrum Meth B*.  
645 2010;**263**:192–199.
- 646 71. Korschinek G, Bergmaier A, Faestermann T, et al. A new value for the half-life of  $^{10}\text{Be}$   
647 by heavy-ion elastic recoil detection and liquid scintillation counting. *Nucl Instrum  
648 Meth B*. 2010;**268**:187–191.
- 649 72. Braucher R, Guillou V, Bourlès DL, et al. Preparation of ASTER in-house  $^{10}\text{Be}/^9\text{Be}$   
650 standard solutions. *Nucl Instrum Meth B*. 2015;**361**:335–340.
- 651 73. Arnold M, Merchel S, Bourlès DL, et al. The French accelerator mass spectrometry  
652 facility ASTER: improved performance and developments. *Nucl Instrum Meth B*.  
653 2010;**268**(11-12):1954–1959.
- 654 74. Borchers B, Marrero S, Balco G, et al. Geological calibration of spallation production  
655 rates in the CRONUS-Earth project. *Quat Geochronol*. 2016;**31**:188–198.
- 656 75. Stone JO. Air pressure and cosmogenic isotope production. *J Geophys Res*.  
657 2000;**105**:23753–23759.
- 658 76. Dunne J, Elmore D, Muzikar P. Scaling factors for the rates of production of  
659 cosmogenic nuclides for geometric shielding and attenuation at depth on sloped  
660 surfaces. *Geomorphology*. 1999;**27**:3–11.
- 661 77. Gosse JC, Phillips FM. Terrestrial in situ cosmogenic nuclides: theory and application.  
662 *Quaternary Sci Rev*. 2001;**20**:1475–560.
- 663 78. Braucher R, Merchel S, Borgomano J, Bourlès DL. Production of cosmogenic  
664 radionuclides at great depth: a multi element approach. *Earth Planet Sci Lett*.  
665 2011;**309**,1–9.

- 666 79. Lal D. Cosmic ray labeling of erosion surfaces: in situ nuclide production rates and  
667 erosion models. *Earth Planet Sci Lett.* 1991;**104**:424–439.
- 668 80. Balco G. Glacier change and paleoclimate applications of cosmogenic-nuclide exposure  
669 dating. *Annu Rev Earth Planet Sci.* 2020;**48**:21–48.
- 670 81. Blomdin R, Stroeven AP, Harbor JM, et al. Evaluating the timing of former glacier  
671 expansions in the Tian Shan: A key step towards robust spatial correlations. *Quaternary*  
672 *Sci Rev.* 2016;**153**:78–96.
- 673 82. Engel Z, Braucher R, Traczyk A, et al. <sup>10</sup>Be exposure age chronology of the last  
674 glaciation in the Krkonoše Mountains, Central Europe. *Geomorphology.* 2014;**206**:107–  
675 121.
- 676 83. Engel Z, Braucher R, AsterTeam. Origin and <sup>10</sup>Be surface exposure dating of a coarse  
677 debris accumulation in the Hrubý Jeseník Mountains, central Europe. *Geomorphology.*  
678 2020;**365**:107292.
- 679 84. Dunai TJ. *Cosmogenic Nuclides.* Cambridge: Cambridge University Press; 2010.
- 680 85. Phillips WM. A review of cosmogenic nuclide surface exposure dating: new challenges  
681 for Scottish geomorphology. *Scott Geogr J.* 2001;**117**:1–15.
- 682 86. Kessler MA, Murray AB, Werner BT, Hallet B. A model for sorted circles as self-  
683 organized patterns. *J Geophys Res.* 2001;**106**(B7):13287–13306.
- 684 87. French H. *The Periglacial Environment.* 4<sup>th</sup> ed. Chichester: Wiley; 2018.
- 685 88. Sekyra J, Sekyra Z. Former existence of a plateau icefield in Bílá louka Meadow,  
686 eastern Giant Mountains: hypothesis and evidence. *Opera Corcon.* 2002;**39**:35–43.
- 687 89. Ludwig, P, Schaffernicht EJ, Shao Y, Pinto JG. Regional atmospheric circulation over  
688 Europe during the Last Glacial Maximum and its links to precipitation. *J Geophys Res-*  
689 *Atmos.* 2016;**121**,2130–2145.
- 690 90. Knotek Z. Geologie Jizerských hor. In: Karpaš R, ed. *Jizerské hory - O mapách, kamení*  
691 *a vodě.* Liberec: Knihy 555; 2009:104–141.
- 692 91. Guido ZS, Ward DJ, Anderson RS. Pacing the post–Last Glacial Maximum demise of  
693 the Animas Valley glacier and the San Juan Mountain ice cap, Colorado. *Geology.*  
694 2007;**35**:739–742.
- 695 92. Prosová M. Studie o periglaciálních zjevech v Hrubém Jeseníku. *Přírodovědecký*  
696 *sborník Ostravského kraje.* 1954;**15**:1–15.
- 697 93. Sekyra J. *Působení mrazu na půdu – kryopedologie se zvláštním zřetelem k ČSR.* Praha:  
698 Nakladatelství Československé Akademie Věd; 1960.

- 699 94. Treml V, Jankovská V, Petr L. Holocene dynamics of the alpine timberline in the High  
700 Sudetes. *Biologia*. 2008;**63**:73–80.
- 701 95. Plug LJ, Gosse JC, McIntosh JJ, Bigley R. Attenuation of cosmic ray flux in temperate  
702 forest. *J Geophys Res*. 2007;**112**:F02022.
- 703 96. Antoine P, Coutard S, Guerin G, et al. Upper Pleistocene loess-palaeosol records from  
704 Northern France in the European context: Environmental background and dating of the  
705 Middle Palaeolithic. *Quatern Int*. 2016;**411**:4–24.
- 706 97. Moseley GE, Spötl C, Svensson A, Cheng H, Brandstätter S, Edwards RL. Multi-  
707 speleothem record reveals tightly coupled climate between central Europe and  
708 Greenland during Marine Isotope Stage 3. *Geology*. 2014;**42**:1043–1046.
- 709 98. Agosta EA, Compagnucci RH. Abrupt Climate Changes During the Marine Isotope  
710 Stage 3 (MIS 3). In: Gasparini G, Rabassa J, Deschamps C, Tonni E, eds. *Marine*  
711 *Isotope Stage 3 in Southern South America, 60 ka B.P.–30 ka B.P.* Cham: Springer;  
712 2016:81–106.
- 713 99. Rasmussen SO, Bigler M, Blockley S, et al. A stratigraphic framework for abrupt  
714 climatic changes during the Last Glacial period based on three synchronized Greenland  
715 ice-core records: refining and extending the INTIMATE event stratigraphy. *Quaternary*  
716 *Sci Rev*. 2014;**106**:14–28.
- 717 100. Seguinot J, Jouvet G, Huss M, Funk M, Ivy-Ochs S, Preusser F. Modelling last glacial  
718 cycle ice dynamics in the Alps. *Cryosphere*. 2018;**12**:3265–3285.
- 719 101. Engel Z, Nývlt D, Křížek M, Treml V, Jankovská V, Lisá L. Sedimentary evidence of  
720 landscape and climate history since the end of MIS 3 in the Krkonoše Mountains, Czech  
721 Republic. *Quaternary Sci Rev*. 2010;**29**:913–927.
- 722 102. Andrieux E, Bateman M, Bertran P. The chronology of Late Pleistocene thermal  
723 contraction cracking derived from sand wedge OSL dating in central and southern  
724 France. *Glob Planet Change*. 2018;**162**:84–100.
- 725 103. Woronko B, Zielinski P, Sokołowski RJ. Climate evolution during the Pleniglacial and  
726 Late Glacial as recorded in quartz grain morphoscopy of fluvial to aeolian successions  
727 of the European Sand Belt. *Geologos*. 2015;**21**:89–103.
- 728 104. Kovács J, Moravcová M, Újvári G, Pintér AG. Reconstructing the paleoenvironment of  
729 East Central Europe in the Late Pleistocene using the oxygen and carbon isotopic signal  
730 of tooth in large mammal remains. *Quatern Int*. 2012;**276–277**:145–154.



- 731 105. Lowe JJ, Rasmussen SO, Björck S, et al. Synchronisation of palaeoenvironmental  
732 events in the North Atlantic region during the Last Termination: a revised protocol  
733 recommended by the INTIMATE group. *Quaternary Sci Rev.* 2008;**27**:6–17.
- 734 106. Lisiecki LE, Raymo MR. A Pliocene-Pleistocene stack of 57 globally distributed  
735 benthic  $\delta^{18}O$  records. *Paleoceanography.* 2005;**20**:PA1003.
- 736 107. Clark PU, Dyke AS, Shakun JD, Carlson AE, Clark J, Wohlfarth B, Mitrovica JX,  
737 Hostetler SW, McCabe AM. The Last Glacial Maximum. *Science.*  
738 2009;**325**(5941):710–713.
- 739 108. Juříčková L, Ložek V, Horáčková J, Tlachač P, Horáček I. Holocene succession and  
740 biogeographical importance of mollusc fauna in the Western Sudetes (Czech Republic).  
741 *Quatern Int.* 2014;**353**:210–224.
- 742 109. Alexandrowicz WP, Ciszek D, Gołas-Siarzewska M. Malacological characteristic of the  
743 Weichselian Upper Pleniglacial (MIS-2) loess profile in Tłumaczów (SW Poland). *Geol*  
744 *Q.* 2013;**57**(3):433–442.
- 745 110. Feurdean A, Perşoiu A, Tanţău I, et al. Climate variability and associated vegetation  
746 response throughout Central and Eastern Europe (CEE) between 60 and 8 ka.  
747 *Quaternary Sci Rev.* 2014;**106**:206–224.
- 748 111. Vandenberghe J, French HM, Gorbunov A, et al. The Last Permafrost Maximum (LPM)  
749 map of the Northern Hemisphere: permafrost extent and mean annual air temperatures,  
750 25–17 ka BP. *Boreas.* 2014;**43**:652–666.
- 751 112. Růžičková E, Zeman A. The Blahutovice-1 borehole near Hranice na Moravě:  
752 weathering effects in Badenian deposits. *Scripta Fac Sci Nat Univ Masaryk Brun Geol.*  
753 1992;**22**:128–132.
- 754 113. Žák K, Richter DK, Filippi M, et al. Coarsely crystalline cryogenic cave carbonate – a  
755 new archive to estimate the Last Glacial minimum permafrost depth in Central Europe.  
756 *Clim Past.* 2012;**8**:1821–1837.
- 757 114. Jahn A. The permafrost active layer in the Sudety Mountains during the last glaciation.  
758 *Quaest Geogr.* 1977;**4**:29–42.
- 759 115. Chmal H, Traczyk A. Plejstocénskie lodowce gruzowe w Karkonoszach. *Czas Geogr.*  
760 1993;**64**(3-4):253–262.
- 761 116. Waroszewski J, Kalinski K, Malkiewicz M, Mazurek R, Kozłowski G, Kabala C.  
762 Pleistocene–Holocene cover-beds on granite regolith as parent material for Podzols—  
763 An example from the Sudeten Mountains. *Catena.* 2013;**104**:161–173.

- 764 117. Traczyk A. Late Pleistocene Evolution of Periglacial and Glacial Relief in the  
765 Karkonosze Mountains. New Hypotheses and Research Perspectives. *Acta U Carol*  
766 *Geogr.* 2004;**39**:59–72.
- 767 118. Christensen NI, Mooney WD. Seismic velocity structure and composition of the  
768 continental crust: A global view. *J Geophys Res.* 1995;**100**(B6):9761–9788.
- 769 119. Small EE, Anderson RS, Repka JL, Finkel R. Erosion rates of alpine bedrock summit  
770 surfaces deduced from in situ <sup>10</sup>Be and <sup>26</sup>Al. *Earth Planet Sci Lett.* 1997;**150**:413–425.
- 771 120. Portenga EW, Bierman PR, Rizzo DM, Rood DH. Low rates of bedrock outcrop erosion  
772 in the central Appalachian Mountains inferred from in situ <sup>10</sup>Be. *GSA Bulletin.*  
773 2013;**125**(1-2):201–215.
- 774 121. Crest Y, Delmas M, Braucher R, Gunnell Y, Calvet M, ASTER Team. Cirques have  
775 growth spurts during deglacial and interglacial periods: Evidence from <sup>10</sup>Be and <sup>26</sup>Al  
776 nuclide inventories in the central and eastern Pyrenees. *Geomorphology.* 2017;**278**:60–  
777 77.
- 778 122. Dethier DP, Lazarus ED. Geomorphic inferences from regolith thickness, chemical  
779 denudation and CRN erosion rates near the glacial limit, Boulder Creek catchment and  
780 vicinity, Colorado. *Geomorphology.* 2006;**75**(3-4):384–399.
- 781 123. Refsnider KA. Dramatic increase in late Cenozoic alpine erosion rates recorded by cave  
782 sediment in the southern Rocky Mountains. *Earth Planet Sci Lett.* 2010;**297**:505–511.
- 783 124. Schaller M, Ehlers TA, Stor T, et al. Spatial and temporal variations in denudation rates  
784 derived from cosmogenic nuclides in four European fluvial terrace sequences.  
785 *Geomorphology.* 2016;**274**:180–192.
- 786 125. Migoń P, Danišik M. Erosional history of the Karkonosze Granite Massif – constraints  
787 from adjacent sedimentary basins and thermochronology. *Geol Quart.* 2012;**56**(3):440–  
788 454.
- 789 126. Herman F, Seward D, Valla PG, et al. Worldwide acceleration of mountain erosion  
790 under a cooling climate. *Nature.* 2013;**504**:146–423.

791 Table 1. Morphological characteristics and <sup>10</sup>Be surface exposure ages for sample boulders.

Sample	Latitude (°N)	Longitude (°E)	Altitude (m a.s.l.)	Boulder length/width/height (m)	Surface aspect /dip (°)	Sample thickness (cm)	Snow depth/duration (cm/month)	Total shielding factor	Production rate (at <sup>-1</sup> g <sup>-1</sup> yr <sup>-1</sup> )	<sup>10</sup> Be concentration (at-1g-1)	<sup>10</sup> Be Age (yr)	Analytical uncertainty (± yr)	Total uncertainty (± yr)	<sup>10</sup> Be max. denudation rate (m/My)	Integration time (yr)
VK-1	50.77646	15.56757	1506	2.2/0.6/0.6	260/2	2	80/6	0.93035	12.93	377,555 ± 14,199	29,244	1100	2071	23.8 ± 0.9	29,032
VK-2	50.77648	15.56754	1503	1.3/0.3/0.5	320/5	5	80/6	0.93035	12.90	288,275 ± 10,354	22,342	802	1562	31.4 ± 1.1	22,218
VK-3	50.77652	15.56754	1506	1.2/0.3/0.7	295/6	5	80/6	0.93035	12.93	242,577 ± 8922	18,740	689	1319	37.5 ± 1.4	18,653
VK-4	50.77690	15.56740	1507	1.1/0.3/0.3	330/10	3	80/6	0.93035	12.94	299,912 ± 10,732	23,177	829	1619	30.2 ± 1.1	23,044
VK-5	50.77691	15.56739	1506	0.8/0.3/0.2	265/12	3	80/6	0.93035	12.93	367,295 ± 14,630	28,444	1133	2048	24.5 ± 1.0	28,243
VK-6	50.77686	15.56731	1507	1.5/0.3/0.2	120/7	6	80/6	0.93035	12.94	391,981 ± 14,423	30,347	1117	2136	22.9 ± 0.8	30,118
LH-1	50.72779	15.68043	1545	0.8/0.6/0.3	125/25	6	80/6	0.93034	13.32	1195,921 ± 36,891	91,318	2817	6161	7.3 ± 0.2	89,266
LH-2	50.72779	15.68046	1544	0.8/0.5/0.2	0/0	6	80/6	0.93034	13.31	817,575 ± 33,737	62,023	2559	4517	10.9 ± 0.5	61,072
LH-3	50.72780	15.68053	1543	0.6/0.3/0.2	195/8	5	80/6	0.93034	13.30	824,325 ± 27,287	62,592	2072	4289	10.8 ± 0.4	61,624
LH-4	50.72753	15.68201	1549	0.9/0.5/0.6	325/3	4	80/6	0.93035	13.36	120,079 ± 74,821	8,955	5580	5606	79.3 ± 49.4	8936
LH-5	50.72751	15.68197	1549	0.8/0.5/0.2	160/7	5	80/6	0.93035	13.36	480,431 ± 16,389	36,074	1231	2490	19.1 ± 0.7	35,750
LH-6	50.72749	15.68203	1546	0.9/0.6/0.3	110/5	3	80/6	0.93035	13.33	803,916 ± 30,423	60,876	2304	4318	11.1 ± 0.4	59,959
BR-1	50.03324	17.18731	1354	0.8/0.2/0.6	240/6	3	55/6	0.95101	12.01	455,811 ± 18,923	38,086	1581	2779	18.2 ± 0.8	37,726
BR-2	50.03330	17.18732	1355	1.4/0.4/0.5	0/0	4	55/6	0.95101	12.02	347,730 ± 12,938	28,967	1078	2045	24.1 ± 0.9	28,758
BR-3	50.03324	17.18719	1354	0.7/0.2/0.4	0/0	5	55/6	0.95101	12.01	272,835 ± 10,804	22,710	899	1633	31.0 ± 1.2	22,582
BR-4	50.03326	17.18737	1354	0.6/0.2/0.5	0/0	7	55/6	0.95101	12.01	311,639 ± 13,077	25,961	1089	1901	27.0 ± 1.1	25,794
BR-5	50.03327	17.18739	1353	0.8/0.2/0.5	0/0	4	55/6	0.95101	12.00	347,506 ± 15,893	28,994	1326	2187	24.1 ± 1.1	28,785
BR-6	50.03330	17.18739	1354	0.6/0.1/0.4	0/0	7	55/6	0.95101	12.01	275,968 ± 11,455	22,972	954	1676	30.6 ± 1.3	22,841
VL-1	50.07115	17.26567	1266	1.6/0.4/1.7	25/5	5	50/5	0.96271	11.46	234,005 ± 9602	20,392	837	1482	34.7 ± 1.4	20,288
VL-2	50.07105	17.26560	1267	1.1/0.5/0.7	0/0	5	50/5	0.96271	11.39	542,127 ± 15,768	47,868	1392	3192	14.4 ± 0.4	47,300

VL-3	50.07115	17.26568	1266	1.8/0.4/1.5	250/4	4	50/5	0.96271	11.33	201,218 ± 7200	17,718	634	1238	40.1 ± 1.4	17,640
VL-4	50.07096	17.26572	1266	1.9/0.3/0.9	145/12	6	50/5	0.96271	11.38	187,172 ± 7019	16,411	615	1161	43.3 ± 1.6	16,344
VL-5	50.07095	17.26580	1266	0.9/0.4/0.7	0/0	6	50/5	0.96271	11.39	270,860 ± 9889	23,773	868	1670	29.6 ± 1.1	23,632
VL-6	50.07091	17.26584	1266	0.9/0.2/0.6	30/12	6	50/5	0.96271	11.33	224,345 ± 8523	19,764	751	1404	35.8 ± 1.4	19,667

792 Table 2. Sample site characteristics and mean <sup>10</sup>Be exposure ages for patterned ground in the Sudetes  
793 Mountains.

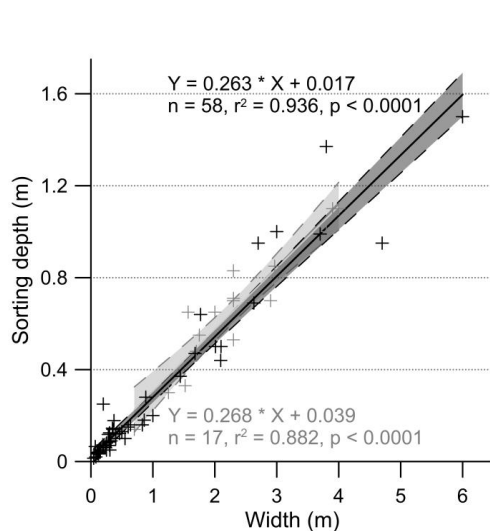
Site	Altitude (m a.s.l.)	Mean/median slope (°)	Elevation relative to local tree line (m)	Bedrock	Density (g/cm <sup>3</sup> )	Mean size of polygon boulders (m)	Montane ecosystem	Vegetation	$\chi^2_R$	SD to mean exposure age (%)	Age clustering (class)	Exposure Age ± uncertainty (kyr)	
												Maximum	Mean
Vysoké Kolo	1503–1507	3/3	+128	fine-grained biotite granite	2.69	0.85	tundra	grasses, lichens	30.7	18	C	30.3 ± 1.1	25.4 ± 1.9
Luční hora	1543–1549	3/2	+143	quartzite	2.65	0.23	tundra	lichens	97.2	52	C	91.3 ± 2.8	53.6 ± 11.4
Břidličná hora	1353–1355	4/4	+30	quartz-rich phyllite	2.73	0.75	tundra	grasses, lichens, dwarf shrubs	21.4	20	C	38.1 ± 1.6	27.9 ± 2.3
Větrná louka	1266–1267	3/3	-87	quartz-rich phyllite	2.73	1.17	forest	spruce forest	123.8	49	C	47.9 ± 1.4	24.3 ± 4.8

Commentaire [Révis3]: Not anymore presented in the text

794  
795 Table 3. Morphology of patterned ground at sample sites.

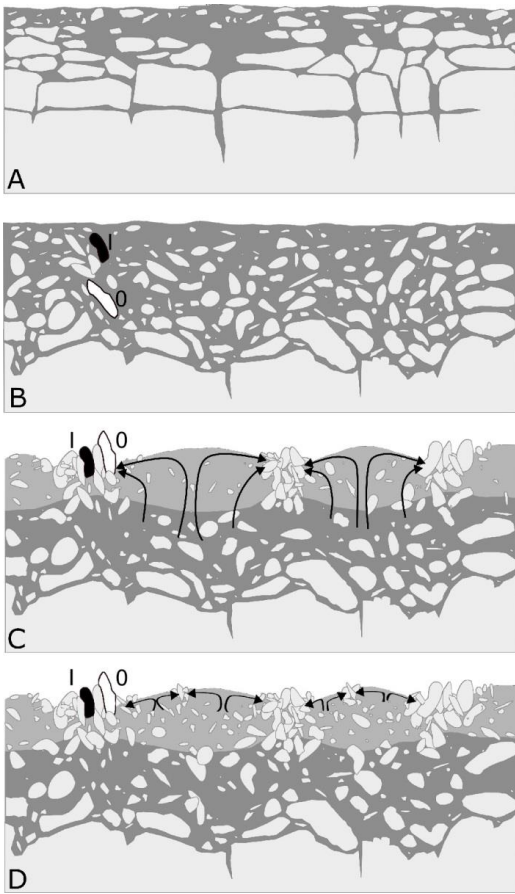
Site	Altitude (m a.s.l.)	Mean length (m)	Mean width (m)	Mean height (m)	Width/Length index	Min–Max Length	Min–Max Width	Min–Max Height	N
Vysoké Kolo	1503–1507	6.97	4.33	0.27	0.64	3.80–10.50	2.50–6.00	0.22–0.34	9
Luční hora	1543–1549	3.67	3.01	0.11	0.83	2.50–5.60	2.10–5.40	0.00–0.30	32
Břidličná hora	1353–1355	5.05	3.88	0.19	0.79	3.20–9.40	2.70–6.40	0.05–0.45	32
Větrná louka	1266–1267	4.76	4.26	1.06	0.91	2.50–6.80	2.30–6.00	0.50–1.50	8

796  
797  
798



800 Figure 4. Width of sorted patterned ground  
801 used to estimate the active-layer thickness.  
802 Black crosses, solid and dashed black lines  
803 indicate the data (from <sup>5, 51–66</sup>), linear fit  
804 and 95% confidence intervals for active  
805 forms. Relict sorted polygons and circles  
806 (grey symbols; data from <sup>4, 9, 63, 67</sup>) reveal  
807 very similar relationship between width  
808 and sorting depth confirming that these  
809 forms are indicative of active layer.  
810

799



811  
 812 Figure 8. Concept of large sorted polygon formation: regolith formation (A), onset of  
 813 differential frost heave and buoyancy-driven clast circulation (B), well-developed forms  
 814 composed of frost-heaved and laterally sorted boulders and finer clasts in the centre (C)<sup>1, 86</sup>,  
 815 formation of small sorted patterns in the fine domain of large sorted polygons (D). Dark and  
 816 light grey colours show a regolith matrix and the central fine domain of polygons,  
 817 respectively. *I* and *O* mark the location of boulders with inherited nuclide component and zero  
 818 inheritance, respectively. Arrows indicate motion of clasts within the fine domain.